

# Rotating $^3\text{He}$ droplets

Martí Pi,<sup>1,2</sup> Francesco Ancilotto,<sup>3,4</sup> and Manuel Barranco<sup>1,2,5</sup>

<sup>1</sup>*Departament FQA, Facultat de Física, Universitat de Barcelona. Diagonal 645, 08028 Barcelona, Spain*

<sup>2</sup>*Institute of Nanoscience and Nanotechnology (IN2UB), Universitat de Barcelona, Barcelona, Spain.*

<sup>3</sup>*Dipartimento di Fisica e Astronomia “Galileo Galilei” and CNISM,  
Università di Padova, via Marzolo 8, 35122 Padova, Italy*

<sup>4</sup>*CNR-IOM Democritos, via Bonomea, 265 - 34136 Trieste, Italy*

<sup>5</sup>*Université Toulouse 3, Laboratoire des Collisions, Agrégats et Réactivité,  
IRSAMC, 118 route de Narbonne, F-31062 Toulouse Cedex 09, France*

(Dated: October 30, 2019)

Motivated by recent experiments, we study normal-phase rotating  $^3\text{He}$  droplets within Density Functional Theory in a semi-classical approach. The sequence of rotating droplet shapes as a function of angular momentum are found to agree with those of rotating classical droplets, evolving from axisymmetric oblate to triaxial prolate to two-lobed shapes as the angular momentum of the droplet increases. Our results, which are obtained for droplets of nanoscopic size, are rescaled to the mesoscopic size characterizing ongoing experimental measurements, allowing for a direct comparison of shapes. The stability curve in the angular velocity-angular momentum plane shows small deviations from the classical rotating drop model predictions, whose magnitude increases with angular momentum. We attribute these deviations to effects not included in the simplified classical model description of a rotating fluid held together by surface tension, i.e. to surface diffuseness, curvature and finite compressibility, and to quantum effects associated with deformation of the  $^3\text{He}$  Fermi surface. The influence of all these effects is expected to diminish as the droplet size increases, making the classical rotating droplet model a quite accurate representation of  $^3\text{He}$  rotation.

## I. INTRODUCTION

Helium is the only element in nature that may condense into macroscopic liquid samples at temperatures close to absolute zero. These systems can be made of either pure isotope, or of  $^3\text{He}$ - $^4\text{He}$  isotopic mixtures. Below a temperature ( $T$ ) that depends on the isotope (2.17 K for  $^4\text{He}$ , 2.7 mK for  $^3\text{He}$ ) and also on the isotopic composition in the case of mixtures,<sup>1</sup> these remarkable fluids undergo a well known normal-to-superfluid phase transition. These properties, which are a manifestation at the microscale of the quantum nature of low temperature liquid helium, have drawn a relentless scientific attention since they were uncovered about 80 years ago. A first hand, personal view of the first stages in the development of helium atoms beams and droplets has been given by J. Peter Toennies.<sup>2</sup>

In more recent years, helium droplets have been the subject of renewed interest, both experimentally and theoretically. In the experiments,  $^4\text{He}$  droplets are produced at  $T \sim 0.37$  K;<sup>4</sup> hence, they are superfluid and represent ideal ultra-cold matrices for spectroscopy studies of captured molecular impurities,<sup>3</sup> and for addressing superfluidity at the nanoscale.<sup>4</sup> At variance,  $^3\text{He}$  droplets are created at  $T \sim 0.15$  K;<sup>5</sup> hence, they are in the normal phase. For this reason, they are expected to behave more as classical viscous fluid droplets.  $^3\text{He}$  droplets have been the subject of far less studies than  $^4\text{He}$  droplets, especially in recent times when the situation has been further aggravated by the prohibitive price of this scarce helium isotope. The activity on  $^3\text{He}$  droplets has been partially reviewed in Refs. 6,7.

Recently, large  $^4\text{He}$  droplets made of  $10^8 - 10^{11}$  atoms

have been created by the hydrodynamic instability of a liquid helium jet passing through the nozzle of the molecular beam apparatus, as reviewed in Ref. 8. Helium drops, which are produced in the normal, non-superfluid phase, may acquire angular momentum during the passage of the fluid through the nozzle, before cooling down and become superfluid. Such droplets could be analyzed one-by-one by x-ray and XUV light and intense high harmonics sources<sup>9,10</sup> which have allowed to determine their shapes and, doping them with Xe atoms,<sup>9,11</sup> the presence of vortices, thus stressing their superfluid nature.

One of the intriguing findings of Refs. 9,10 was that the sequence of shapes of the spinning superfluid  $^4\text{He}$  droplets is in accordance with that of classical rotating droplets.<sup>12-15</sup> It has been shown that it is the presence of quantized vortices that confers to the superfluid droplets the appearance of classical viscous droplets when they are set in rotation.<sup>16</sup>

It is quite natural to ask whether droplets made of liquid  $^3\text{He}$  do indeed rotate as classical droplets made of normal fluid, and whether their properties may be described by a more microscopic approach, instead of that successfully used for viscous liquid droplets.<sup>12-15</sup> Besides, a proper microscopic description of pristine  $^3\text{He}$  droplets is a necessary step towards the study of mixed  $^3\text{He}$ - $^4\text{He}$  droplets, which represent the prototype of strongly correlated Bose-Fermi liquid mixtures. These are the goals of the present paper, that accompanies an experimental one on rotating large  $^3\text{He}$  droplets.<sup>17</sup>

In this work we describe deformed droplets within a Density Functional Theory (DFT) formalism for liquid  $^3\text{He}$ .<sup>18</sup> At the experimental temperatures, thermal effects on the energetics and morphology of the droplet are

negligible,<sup>19</sup> so we shall use a  $T = 0$  method. Zero temperature means here a very low temperature, but above the  $\sim 2.7$  mK at which  $^3\text{He}$  becomes superfluid.

As  $^3\text{He}$  atoms are fermions, the DFT-Kohn-Sham (DFT-KS) approach should be the method of choice for this study. It has been used in the past to address spherical  $^3\text{He}$  droplets made of up to a few hundred atoms.<sup>20</sup> Deformed (doped)  $^3\text{He}$  droplets with a few tens of  $^3\text{He}$  atoms have been addressed as well within such approach.<sup>19</sup> Let us mention that Diffusion Monte Carlo calculations have been made for pure  $^3\text{He}_N$  droplets up to  $N = 34$ ,<sup>21</sup> and exact diagonalization results exist for  $^3\text{He}_4$  clusters doped with  $\text{Cl}_2$ .<sup>22</sup>

Unfortunately, the DFT-KS approach is unfeasible for large, deformed  $^3\text{He}$  droplets as the ones investigated here. The use of a DFT-KS scheme is unavoidable when shell effects are expected to play a role, as in small droplets;<sup>6,19</sup> but for the experimental droplet sizes, of the order of  $10^8 - 10^{10}$  atoms,<sup>17</sup> the shell structure cannot play any substantial role. Besides, temperatures of the order of 100 mK have been found to wash out the shell structure of mixed  $^3\text{He}$ - $^4\text{He}$  droplets.<sup>23</sup> Under these conditions, the use of a semiclassical approximation to the DFT formalism, as the one described in the following, is fully justified. The finite viscosity of  $^3\text{He}$  at the experimental temperatures adds further justification to using classical or semiclassical methods to address rotating  $^3\text{He}$  droplets.

We have thus resorted to a semiclassical approach, treating the  $^3\text{He}$  droplets in the DFT plus rotating Thomas-Fermi (TF) framework, which has been successfully used in Nuclear Physics to address deformed nuclei.<sup>24-26</sup> The DFT-TF method is the only realistic framework that has the virtue of making numerical simulations affordable and that can be extended in a natural way to mixed helium droplets at the experimental conditions.<sup>6</sup>

This work is organized as follows. In Sec. II we present the DFT-TF method used to describe the  $^3\text{He}$  droplets. The results are discussed in Sec. III, and a summary and outlook are given in Sec. IV. Details on the rotating TF approximation are given in the Appendix.

## II. MODEL

Within DFT, the total energy  $E$  of a  $^3\text{He}_N$  droplet at zero temperature is written as a functional  $\mathcal{E}_c$  of the  $^3\text{He}$  atom density  $\rho$ , here taken from Ref. 27:

$$E[\rho] = \int d\mathbf{r} \frac{\hbar^2}{2m^*} \tau + \int d\mathbf{r} \mathcal{E}_c[\rho] \quad (1)$$

The first term is the kinetic energy of  $^3\text{He}$  with an effective mass  $m^*$ , and  $\tau$  is the kinetic energy density, both depending on  $\rho$ . In the TF approximation of Ref. 27 (see also Ref. 18),

$$\tau = \frac{3}{5} (3\pi^2)^{2/3} \rho^{5/3} + \frac{1}{18} \frac{(\nabla\rho)^2}{\rho} \quad (2)$$

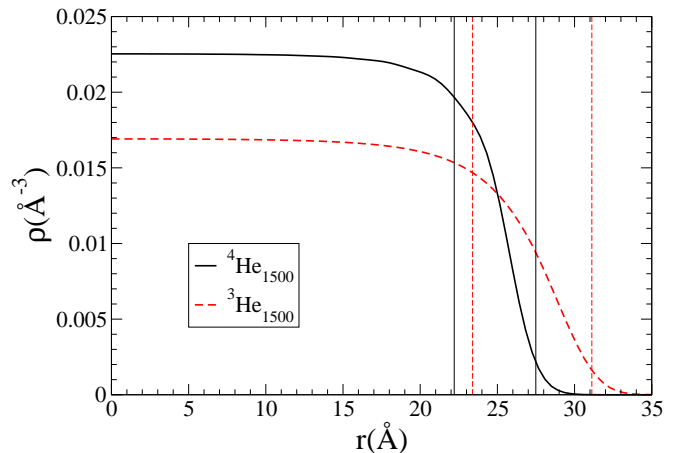


FIG. 1: Density profile of the  $^3\text{He}_{1500}$  and  $^4\text{He}_{1500}$  spherical droplets. The region between the thin vertical lines is the surface region defined as that where the helium density falls from  $0.9 \times \rho_0$  to  $0.1 \times \rho_0$ .

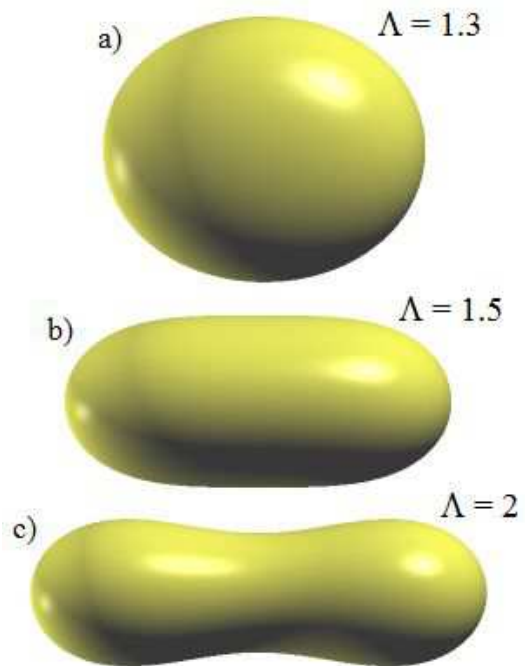


FIG. 2: Some prolate  $^3\text{He}_{1500}$  equilibrium configurations represented by their sharp density surfaces (not to scale).

The second term in the previous equation is a Weizsäcker-type gradient correction which is necessary in order to have helium densities with an exponential fall-off at the surface.<sup>28</sup> The energy functional Eq. (1) together with the TF approximation Eq. (2) have been found to accurately reproduce the equation of state of the homogeneous system and the correct value for the  $^3\text{He}$  surface tension<sup>27</sup>.

In this work, the number of  $^3\text{He}$  atoms is fixed to  $N = 1500$ . The droplet equilibrium configuration is obtained

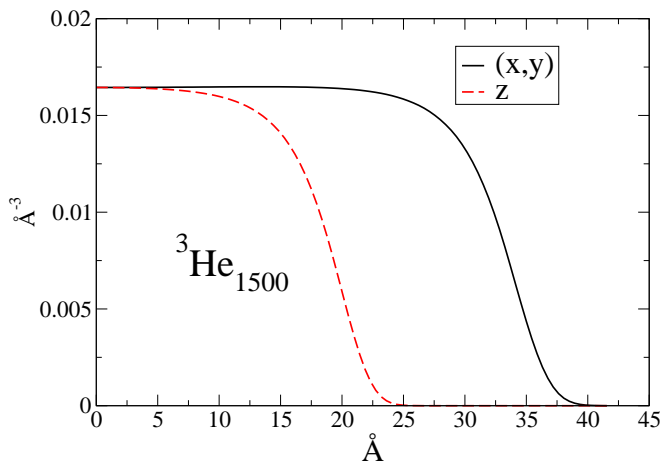


FIG. 3: Density profile of the oblate  $\Omega = 0.6364$  configuration along the  $x$  and  $y$  axes (black, solid line), and along the rotation  $z$ -axis (red, dashed line). The densities have reflective symmetry with respect to the coordinate planes.

by solving the Euler-Lagrange (EL) equation arising from functional variation of Eq. (1)

$$\frac{\delta}{\delta \rho} \left\{ \frac{\hbar^2}{2m^*} \tau + \mathcal{E}_c \right\} = \mu \quad (3)$$

where  $\mu$  is the  $^3\text{He}$  chemical potential. Defining  $\Psi = \sqrt{\rho}$ , Eq. (3) can be written as a Schrödinger-like equation<sup>27</sup>

$$\mathcal{H}[\rho] \Psi = \mu \Psi \quad (4)$$

where  $\mathcal{H}$  is the one-body effective Hamiltonian that results from the functional variation.

When the rotating droplet –made of fermions in the normal phase– is addressed in the TF approximation, the Fermi sphere is shifted by the motion of the droplet as a whole; this adds to the droplet total energy a rotational term that has the rigid body appearance<sup>24</sup>

$$E[\rho] \rightarrow \mathcal{R}[\rho] = E[\rho] + \frac{1}{2} \mathcal{I} \omega^2 \quad (5)$$

where  $\mathcal{R}[\rho]$  is the Routhian of the system and  $\mathcal{I}$  is defined in Eq. (7) below. Details are given in the Appendix.

To deposit angular momentum in a droplet rotating with angular velocity  $\omega$  about a given axis (the  $z$ -axis here), it is convenient to work in the fixed-droplet frame of reference (corotating frame at angular velocity  $\omega$ ), *i.e.* we consider

$$E'[\rho] = \mathcal{R}[\rho] - \hbar \omega \langle L \rangle = E[\rho] - \frac{1}{2} \mathcal{I} \omega^2 \quad (6)$$

where  $\hbar \langle L \rangle = \mathcal{I} \omega$  is the  $^3\text{He}$  angular momentum obtained from the classical rigid body moment of inertia  $\mathcal{I}$

$$\mathcal{I} = m \int d\mathbf{r} (x^2 + y^2) \rho(\mathbf{r}) \quad (7)$$

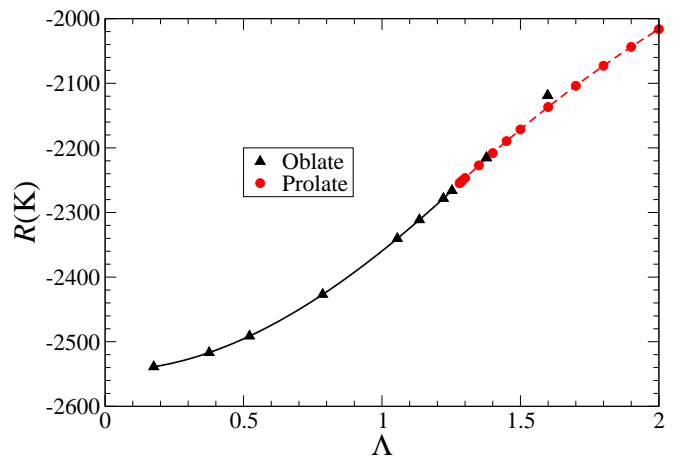


FIG. 4: Routhian  $\mathcal{R}[\rho]$  as a function of  $\Lambda$ . Black triangles: oblate configurations. Open triangles are metastable oblate configurations. Red circles: prolate configurations. The lines are cubic splines of the calculated points.

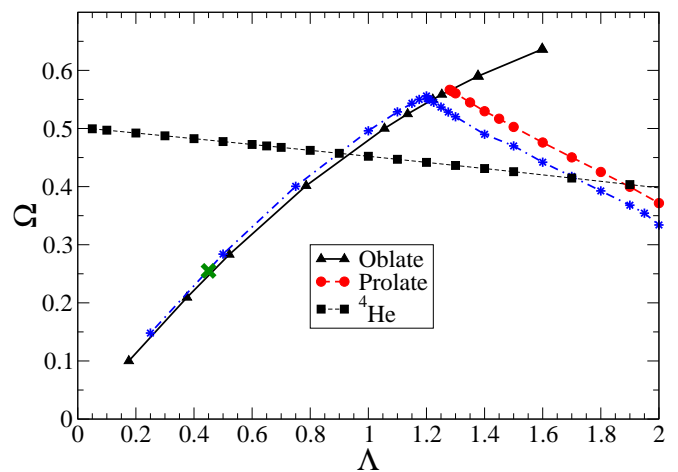


FIG. 5: Rescaled angular velocity  $\Omega$  *vs.* rescaled angular momentum  $\Lambda$ . Black triangles: oblate configurations. Red circles: prolate configurations. Open triangles are metastable oblate configurations. The lines are cubic splines of the displayed points. The stars connected with a blue dot-dashed line is the classical rotating drop result of Ref. 14, and the big green cross represents the average experimental value given in Fig. 5 of Ref. 17. For the sake of comparison, the  $\Omega(\Lambda)$  curve corresponding to vortex-free  $^4\text{He}$  droplets is also shown (black squares).

We want to stress that the rigid-body moment of inertia is not an imposed ingredient to the DFT-TF framework. It arises naturally from the TF approximation as shown in the Appendix. In the more general DFT-KS framework, the rigid-body moment of inertia similarly appears within the so-called “cranking model”, as thoroughly discussed for nucleons rotating in the mean field created by the atomic nucleus.<sup>29–31</sup>

In the corotating frame, we have to look for solutions of the EL equation resulting from the functional variation

of  $E'[\rho]$ :

$$\left\{ \mathcal{H}[\rho] - \frac{m}{2} \omega^2 (x^2 + y^2) \right\} \Psi(\mathbf{r}) = \mu \Psi(\mathbf{r}). \quad (8)$$

The results presented in this work have been obtained adapting the 4He-DFT BCN-TLS computing package<sup>32</sup> to the case of  $^3\text{He}$  atoms in the TF approximation. Details on how Eqs. (3) and (8) are solved can be found in Refs. 7,33 and references therein. In short, we work in Cartesian coordinates, make extensive use of the Fast-Fourier Transform to compute the convolutions entering the definition of the effective Hamiltonian  $\mathcal{H}$ , and obtain the droplet equilibrium configuration by imaginary-time relaxation. To determine the prolate branch we have iterated on  $\omega$  to get the desired  $L_z$  value.<sup>12-14,16</sup>

The experimental droplets have a radius in the 100-200 nm range.<sup>17</sup> A comparison between the calculated nanoscopic DFT droplets and the experimental ones thus requires some scaling procedure. To this end, we have introduced a dimensionless angular momentum  $\Lambda$  and angular velocity  $\Omega$  as done for classical drops<sup>12-14</sup>

$$\Omega \equiv \sqrt{\frac{m \rho_0 R^3}{8 \gamma}} \omega = \left[ \frac{2m}{\hbar^2} \frac{3}{64\pi\gamma} N \right]^{1/2} \hbar\omega \quad (9)$$

$$\Lambda \equiv \frac{\hbar}{\sqrt{8\gamma R^7 m \rho_0}} L_z = \left[ \frac{\pi}{3\gamma r_0^4} \frac{\hbar^2}{2m} \right]^{1/2} \frac{L_z}{N^{7/6}}$$

In the above expressions,  $\gamma$  and  $\rho_0$  are the surface tension and liquid atom density at zero temperature and pressure,  $R$  is the sharp radius of the spherical droplet when  $L_z = 0$ , and  $r_0$  is the bulk radius defined such that  $4\pi r_0^3 \rho_0 / 3 = 1$ , hence  $R = r_0 N^{1/3}$ . For liquid  $^3\text{He}$ , these values are  $\gamma = 0.113 \text{ K } \text{\AA}^{-2}$  and  $\rho_0 = 0.0163 \text{ \AA}^{-3}$  ( $r_0 = 2.45 \text{ \AA}$ ). Besides,  $\hbar^2/m = 16.08 \text{ K } \text{\AA}^2$ . Liquid helium is fairly incompressible and hence the volume of the deformed configurations is also taken as  $V = 4\pi R^3/3$ .

In classical model approaches,<sup>12-14</sup> it is assumed that the equilibrium configuration of the rotating droplet is solely determined by the balance between the rotational and surface energies. This makes the problem amenable to a dimensionless formulation, where the Routhian can be expressed in terms of the  $\Lambda$  and  $\Omega$  variables which characterize the equilibrium configuration irrespective of the droplet size and consequently the results are universal. This is quite not so in microscopic approaches such as DFT for instance, where the droplets have a large but finite incompressibility, and also a surface finite width instead of a sharp interface separating the fluid from the vacuum as assumed in classical models. In general, not only surface and rotational energies matter to determine the shape of the droplet at equilibrium; volume and quantum kinetic energy terms do change with deformation and this must be taken into account, as the present DFT approach does. Curvature energy, naturally incorporated in the DFT approach, contributes as well to the energy of the droplet, and its effect increases with the droplet deformation, thus likely affecting the location of the higher

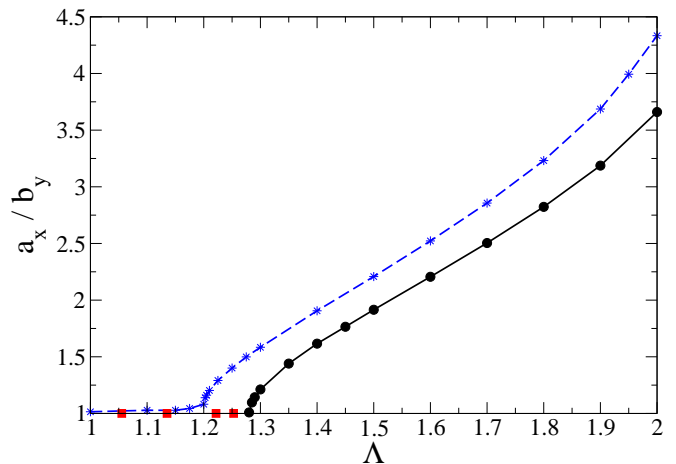


FIG. 6: Aspect-ratio  $AR = a_x/b_y$  curve vs.  $\Lambda$  for  $^3\text{He}$ .  $AR = 1$  correspond to oblate configuration. The starred symbols connected by a dashed blue line are the classical model results.<sup>15</sup>

angular momentum equilibrium configurations in the  $\Lambda$ - $\Omega$  plane.

Consequently, some differences are expected to show up when comparing the results obtained in classical and DFT approaches, especially for small drops for which the surface thickness is not negligible compared to their radius. This is shown in Fig. 1 for the  $^3\text{He}_{1500}$  and  $^4\text{He}_{1500}$  droplets as well. The  $^3\text{He}$  surface is thicker as a natural consequence of the the quantum zero point motion, which is larger for  $^3\text{He}$  than of  $^4\text{He}$  because its mass is smaller. Experiments on the free surface of liquid  $^4\text{He}$  films adsorbed on a solid substrate at  $T = 0.45 \text{ K}$  have yielded surface widths between  $5.3 \pm 0.5 \text{ \AA}$  (thin films) and  $6.5 \pm 0.5 \text{ \AA}$  (thick films).<sup>34</sup>

For any stationary configuration obtained solving Eq. (8), a sharp density surface is determined by calculating the locus at which the helium density equals  $\rho_0/2$ ; for a spherical distribution this corresponds to a sphere of radius  $R = r_0 N^{1/3}$ . In the case of deformed droplets, three lengths are introduced corresponding to the distances from the center of mass (COM) of the droplet to the sharp surface along the rotation axis ( $c_z$ ), the largest distance from the COM to the sharp surface along an axis perpendicular to the rotation axis ( $a_x$ ), and the distance of the COM to the sharp surface in the direction perpendicular to the other two ( $b_y$ ). One expects,<sup>35</sup> and our calculations confirm, that  $a_x \geq b_y > c_z$ .

### III. RESULTS

Table I collects the relevant features of the calculated stationary configurations.

Figure 2 shows three characteristic prolate  $^3\text{He}_{1500}$  droplets whose shapes evolve from ellipsoidal to capsule-like to two-lobed as angular momentum increases. It is worth mentioning that vortex-free  $^4\text{He}$  droplet configura-

	$\Lambda$	$\Omega$	$a_x$ (Å)	$b_y$ (Å)	$c_z$ (Å)	$AR$	$b_y^3/V$	$a_x/c_z$	$\mathcal{I}/\mathcal{I}_{sph}$	$\mathcal{R}$ (K)
O	0.1755	0.1000	28.15	28.15	27.88	1	0.242	1.010	1.045	-2538.86
O	0.3759	0.2093	28.47	28.47	27.26	1	0.251	1.044	1.069	-2516.80
O	0.5216	0.2832	28.83	28.83	26.59	1	0.260	1.084	1.096	-2491.30
O	0.7858	0.4015	29.68	29.68	25.01	1	0.284	1.187	1.165	-2426.83
O	1.0553	0.5000	30.76	30.76	23.12	1	0.316	1.330	1.256	-2340.33
O	1.1352	0.5250	31.10	31.10	22.53	1	0.327	1.380	1.287	-2311.30
O	1.2217	0.5500	31.49	31.49	21.89	1	0.339	1.439	1.322	-2278.32
O	1.2527	0.5585	31.63	31.63	21.66	1	0.344	1.460	1.335	-2266.12
O	1.2800	0.5665	31.71	31.71	21.47	1	0.347	1.477	1.345	-2254.65
O*	1.3774	0.5900	32.21	32.21	20.72	1	0.363	1.555	1.389	-2215.34
O*	1.5984	0.6364	33.28	33.28	19.05	1	0.401	1.747	1.495	-2119.10
P	1.2800	0.5665	31.85	31.56	21.47	1.009	0.345	1.483	1.345	-2254.65
P	1.2850	0.5652	33.21	30.27	21.43	1.097	0.301	1.550	1.353	-2252.65
P	1.2900	0.5637	33.89	29.65	21.39	1.143	0.283	1.584	1.362	-2250.65
P	1.3000	0.5605	34.89	28.79	21.30	1.212	0.259	1.638	1.380	-2246.66
P	1.3500	0.5448	37.98	26.37	20.89	1.440	0.199	1.818	1.474	-2227.06
P	1.4000	0.5296	40.17	24.85	20.47	1.616	0.167	1.963	1.573	-2208.02
P	1.4500	0.5168	41.89	23.74	20.07	1.765	0.145	2.088	1.670	-2201.98
P	1.5000	0.5027	43.52	22.73	19.64	1.915	0.128	2.216	1.776	-2171.43
P	1.6000	0.4759	46.40	21.03	18.80	2.206	0.101	2.467	2.001	-2136.74
P	1.7000	0.4503	48.98	19.56	17.94	2.504	0.0813	2.730	2.247	-2103.91
P	1.8000	0.4252	51.37	18.20	17.02	2.823	0.0655	3.018	2.519	-2072.87
P	1.9000	0.3997	53.66	16.84	16.01	3.187	0.0519	3.352	2.829	-2043.62
P	2.0000	0.3716	55.96	15.29	14.75	3.660	0.0389	3.795	3.203	-2016.24

TABLE I: Characteristics of the rotating  ${}^3\text{He}_{1500}$  droplet configurations calculated in this work. O: oblate configurations; P: prolate configurations. O\*: metastable oblate configurations.  $\Lambda$  and  $\Omega$  are the dimensionless angular momentum and velocity, and  $\mathcal{R}$  is the Routhian.  $AR$  is the aspect ratio  $AR = a_x/b_y$  ( $AR = 1$  for oblate configurations), and  $\mathcal{I}/\mathcal{I}_{sph}$  is the DFT moment of inertia in units of that of a sphere of sharp radius,  $\mathcal{I}_{sph} = (2/5)m r_0^2 N^{5/3}$ ; see the text for the meaning of the other entries.

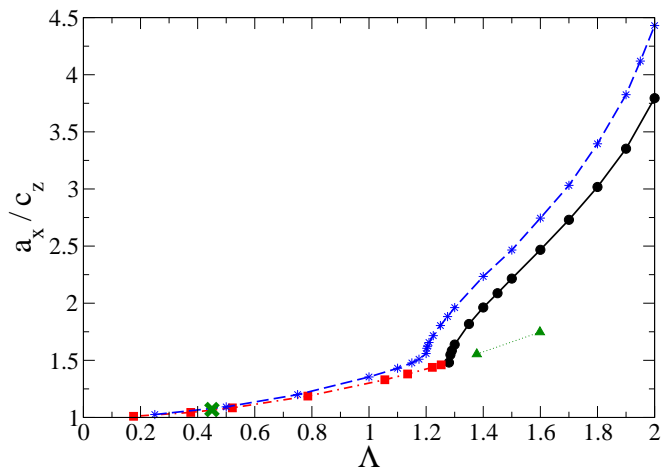


FIG. 7: Aspect-ratio  $a_x/c_z$  curve vs.  $\Lambda$  for  ${}^3\text{He}$ . Red squares correspond to oblate configurations, and black dots to prolate configurations. Green triangles correspond to metastable oblate configurations. The starred symbols connected by a dashed blue line are the classical model results,<sup>15</sup> and the big green cross represents the average experimental value given in Fig. 5 of Ref. 17.

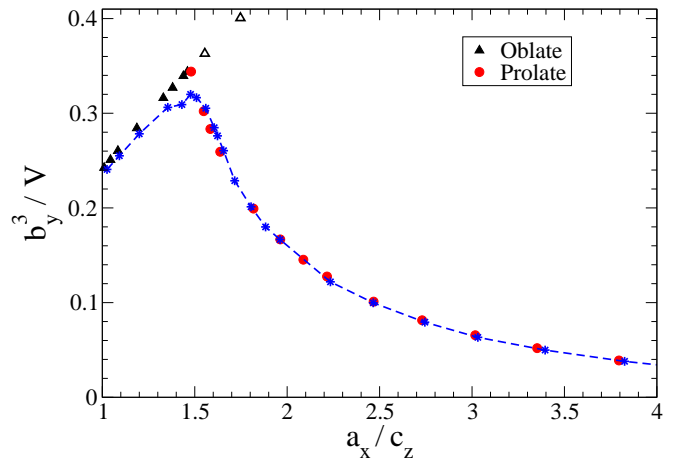


FIG. 8: Aspect-ratio  $b_y^3/V$  vs.  $a_x/c_z$  curve for  ${}^3\text{He}$ . Black triangles: oblate configurations. Open triangles are metastable oblate configurations. Red circles: prolate configurations. The starred symbols connected by a dashed blue line are the classical model results.<sup>15</sup>

tions are more stretched than  ${}^3\text{He}$  ones for the the same

$\Lambda$  value. In particular, the  $\Lambda = 1.5$   ${}^4\text{He}$  configuration is already two-lobed and has  $a_x/c_z = 3.578$ , see the Supporting Material of Ref. 16. This is due to the superfluid character of the  ${}^4\text{He}$  droplets. In the absence of vortex arrays, only capillary waves can carry angular momentum and this requires larger deformations than in the  ${}^3\text{He}$  case.

Blood-cell shapes (i.e. oblate droplets thinner in the center and thicker at the periphery) have been observed for spheroidal  ${}^4\text{He}$  droplets beyond the classical stability limit.<sup>9</sup> Metastable oblate  ${}^3\text{He}$  droplets display a minute depletion at their center, as can be seen in Fig. 3 for the largest angular velocity considered in our calculations,  $\Omega = 0.6364$ .

To determine the oblate-to-prolate bifurcation point, one has to compare the Routhian  $\mathcal{R}[\rho]$  of the oblate and prolate configurations for the same  $\Lambda$  value; the configuration with the smaller  $\mathcal{R}$  is the equilibrium one.<sup>12</sup> Within the classical model approach to droplets subject only to surface tension and centrifugal forces, the bifurcation point is  $(\Omega_{cl}, \Lambda_{cl}) = (0.55, 1.20)$ .<sup>12,13,15</sup> Within the DFT-TF approach to  ${}^3\text{He}$  droplets, the bifurcation point is at  $(\Omega, \Lambda) \sim (0.57, 1.28)$ , as can be seen from Fig. 4.

Figure 5 shows the rescaled angular velocity  $\Omega$  vs. rescaled angular momentum  $\Lambda$ . For a fixed  $\Omega$ , the DFT result is shifted to the right of the classical one. The existence of a surface width is expected to produce some shift. Indeed, due to the density spill-out beyond the sharp density surface, droplets described realistically have more fluid away from the rotation axis than if the surface is sharp as in classical models. Hence, for a given  $\Omega$ , DFT configurations must have a larger moment of inertia and thus a larger  $\Lambda$  value.<sup>36</sup>

Figure 5 also shows the  $\Omega(\Lambda)$  relationship for vortex-free  ${}^4\text{He}$  droplets –where angular momentum is associated to giant capillary waves– obtained in Ref. 16. It is worth seeing the completely different behavior between a rotational ( ${}^3\text{He}$ ) and an irrotational –potential– fluid (superfluid  ${}^4\text{He}$ ).

The cross in the oblate branch in Figs. 5 and 7 shows the experimental average value measured for  $10^8 - 10^{11}$  atoms  ${}^3\text{He}$  droplets,<sup>17</sup> indeed confirming the predictions of our calculations and the validity of the classical rigid-body model for  ${}^3\text{He}$  rotation.

Figure 6 shows  $AR$  as a function of  $\Lambda$  extracted from the information in Table I. For comparison, the classical result is also shown.<sup>14</sup> Figure 7 shows the aspect ratio  $a_x/c_z$  as a function of  $\Lambda$ .

We recall that the diffraction images that are observed in experiments on spinning  ${}^3\text{He}$  droplets do not allow to obtain the droplet image in the direction perpendicular to the detector plane.<sup>17</sup> Angular momentum is also a key quantity that has eluded *direct* experimental determination for  ${}^4\text{He}$ <sup>9,10</sup> and  ${}^3\text{He}$  droplets as well.<sup>17</sup> When the diffraction images correspond to droplets that have been unambiguously detected with their rotation axis aligned with the x-ray beam,<sup>9,37</sup> the calculated aspect ratio  $AR = a_x/b_y$  as a function of  $\Lambda$  might allow to de-

termine the angular momentum of the droplet using the classical or DFT-TF calculations. The fact that both approaches sensibly yield the same  $\Omega(\Lambda)$  relationship in the oblate branch renders this model-dependent procedure to determine the angular momentum and velocity of oblate  ${}^3\text{He}$  droplets very reliable up to fairly large  $\Lambda$  values.

Our results confirm that the diffraction images of Fig. 2(b) and (c) of Ref. 17 indeed represent ellipsoidal and capsule-like droplet shapes, respectively; roughly, they correspond to Fig 2 b) and c) of this work. The droplet with the largest  $AR$  detected in the experiment (1.99) correspond to a two-lobed shape, as shown in Fig. 2 c).

As mentioned, so far there is no direct experimental information on the angular momentum of the rotating droplets, and the rotational axis has been determined only in a few cases. The shape of  ${}^4\text{He}$  droplets has been determined parametrizing them and computing the wide-angle diffraction patterns they produce, iteratively changing the parameters until matching the experimental diffraction patterns.<sup>10</sup> This procedure does not provide the angular momentum nor the direction of the rotation axis, but supplies interesting information, in particular the distance of the COM to the droplet surface along the axes used to describe the parametrized droplet surface. This is the rationale for displaying  $b_y^3/V$  vs. the ratio  $a_x/c_z$  in Fig. 8; when  $a_x/c_z = 1$ ,  $b_y^3/V = R^3/V = 3/(4\pi)$ , that can be used to compare the classical and DFT results. The dashed line shows the classical model result of Ref. 15. The agreement between classical and DFT-TF calculations for  ${}^3\text{He}$  droplets is good, and even remarkable for prolate configurations. A similar good agreement was found between parametrized, vortex-hosting DFT, and classical  ${}^4\text{He}$  droplets.<sup>10,16</sup>

#### IV. SUMMARY AND OUTLOOK

We have studied rotating  ${}^3\text{He}$  droplets combining a semiclassical Thomas-Fermi approach with the well established DFT formalism. We have shown that classical models for the equilibrium shapes of rotating drops which are subject to surface tension and centrifugal forces alone work remarkably well when they are applied to nanoscopic quantum object as  ${}^3\text{He}$  droplets. Minor differences appear between their results and the DFT ones that are likely due to a better description of the droplet surface and to quantum kinetic energy contributions in the microscopic approach that, together with curvature energy and compressibility effects, are lacking in classical models.

The DFT approach to rotating helium nanodroplets has been previously applied to isotopically pure  ${}^4\text{He}$  superfluid droplets, allowing to clarify the influence of vortex arrays on their equilibrium shapes and disclosing the presence of capillary waves and their interplay with vortices.<sup>16,39</sup> We have shown here that the DFT approach allows to describe as well rotating quantum normal fluid  ${}^3\text{He}$  droplets on a microscopic and firm basis. The avail-

ability of an accurate theoretical framework for studying spinning droplets of both isotopes is a crucial ingredient necessary for addressing a far more challenging system, namely rotating mixed  $^3\text{He}$ - $^4\text{He}$  droplets at very low temperatures, a work that is now in progress.

### Acknowledgments

We thank Andrey Vilesov and Luis Egido for useful discussions and exchanges. We are most indebted to Sam Butler for providing us with the results of the classical model calculations. This work has been performed under Grant No FIS2017-87801-P (AEI/FEDER, UE). M. B. thanks the Université Fédérale Toulouse Midi-Pyrénées for financial support throughout the ‘‘Chaires d’Attractivité 2014’’ Programme IMDYNHE

### Appendix

We introduce in this Appendix the basics of the rotating TF model, as discussed in Ref. 24. In a rotating  $^3\text{He}$  droplet, the local momentum distribution of its atoms is altered due to the motion of the droplet as a whole. The Fermi sphere is displaced from  $\mathbf{k} = 0$

$$|\mathbf{k}(\mathbf{r}) - \mathbf{K}_R(\mathbf{r})| \leq k_F(\mathbf{r}) \quad (\text{A.1})$$

where  $\hbar\mathbf{k}_F(\mathbf{r})$  is the Fermi momentum at point  $\mathbf{r}$  and  $\hbar\mathbf{K}_R(\mathbf{r})$  is the local momentum due to rotation, namely

$$\mathbf{K}_R(\mathbf{r}) = \frac{m}{\hbar}\boldsymbol{\omega} \times \mathbf{r} \quad (\text{A.2})$$

It is straightforward to obtain the expressions for quantities such as the particle number  $N$

$$N = \frac{2}{(2\pi)^3} \int d\mathbf{r} \int_{|\mathbf{k}(\mathbf{r}) - \mathbf{K}_R(\mathbf{r})| \leq k_F(\mathbf{r})} d\mathbf{k} = \frac{1}{3\pi^2} \int d\mathbf{r} k_F^3(\mathbf{r}) \quad (\text{A.3})$$

Thus the particle density is

$$\rho(\mathbf{r}) = \frac{k_F^3(\mathbf{r})}{3\pi^2} \Rightarrow k_F(\mathbf{r}) = [3\pi^2 \rho(\mathbf{r})]^{1/3} \quad (\text{A.4})$$

The kinetic energy is similarly obtained

$$T = \frac{2}{(2\pi)^3} \int d\mathbf{r} \int_{|\mathbf{k}(\mathbf{r}) - \mathbf{K}_R(\mathbf{r})| \leq k_F(\mathbf{r})} d\mathbf{k} \frac{\hbar^2 k^2}{2m} \quad (\text{A.5})$$

As done in Eq. (A.3) for  $N$ , if  $\mathbf{k}(\mathbf{r}) - \mathbf{K}_R(\mathbf{r}) \equiv \mathbf{k}'(\mathbf{r})$ , the Jacobian is  $|J| = 1$  and the kinetic energy becomes

$$T = \frac{\hbar^2}{2m} \int d\mathbf{r} \frac{2}{(2\pi)^3} \int_{|\mathbf{k}'(\mathbf{r})| \leq k_F(\mathbf{r})} d\mathbf{k}' [k'^2 + K_R^2] \quad (\text{A.6})$$

(the integral of the cross term  $2\mathbf{k}'(\mathbf{r}) \cdot \mathbf{K}_R(\mathbf{r})$  is zero). Hence,

$$T = \frac{\hbar^2}{2m} \int d\mathbf{r} \frac{2}{(2\pi)^3} \left[ \frac{4\pi}{5} k_F^5(\mathbf{r}) + K_R^2(\mathbf{r}) \frac{4\pi}{3} k_F^3(\mathbf{r}) \right] \quad (\text{A.7})$$

and

$$T = \frac{\hbar^2}{2m} \int d\mathbf{r} \frac{3}{5} (3\pi^2)^{2/3} \rho^{5/3}(\mathbf{r}) + \frac{\hbar^2}{2m} \int d\mathbf{r} K_R^2(\mathbf{r}) \rho(\mathbf{r}) \quad (\text{A.8})$$

The first term is the ordinary TF kinetic energy. The second term is easily identified with the rotation energy. If we take  $\boldsymbol{\omega}$  in the  $z$  direction [ $\boldsymbol{\omega} = \omega(0, 0, 1)$ ] and substitute  $\mathbf{K}_R(\mathbf{r})$  by its expression Eq. (A.2) one gets

$$\frac{\hbar^2}{2m} \int d\mathbf{r} K_R^2(\mathbf{r}) \rho(\mathbf{r}) = \frac{1}{2} m \omega^2 \int d\mathbf{r} (x^2 + y^2) \rho(\mathbf{r}) \equiv \frac{1}{2} \mathcal{I} \omega^2 \quad (\text{A.9})$$

where we have introduced the definition of the moment of inertia  $\mathcal{I}$  about the  $z$  axis. It is worth seeing that the TF approximation leads naturally to a rigid-body rotation in the case of fermions.

Let us calculate the angular momentum

$$\begin{aligned} \mathbf{L} &= \frac{2}{(2\pi)^3} \hbar \int d\mathbf{r} \int_{|\mathbf{k}(\mathbf{r}) - \mathbf{K}_R(\mathbf{r})| \leq k_F(\mathbf{r})} d\mathbf{k} (\mathbf{r} \times \mathbf{k}) \quad (\text{A.10}) \\ &= \frac{2}{(2\pi)^3} \hbar \int d\mathbf{r} \int_{|\mathbf{k}'(\mathbf{r})| \leq k_F(\mathbf{r})} d\mathbf{k}' \mathbf{r} \times [\mathbf{k}' + \mathbf{K}_R(\mathbf{r})] \\ &= \hbar \int d\mathbf{r} [\mathbf{r} \times \mathbf{K}_R(\mathbf{r})] \rho(\mathbf{r}) = m \int d\mathbf{r} [\mathbf{r} \times (\boldsymbol{\omega} \times \mathbf{r})] \rho(\mathbf{r}) \end{aligned}$$

In cartesian coordinates,

$$\mathbf{r} \times (\boldsymbol{\omega} \times \mathbf{r}) = \omega[-xz\hat{i} - yz\hat{j} + (x^2 + y^2)\hat{k}] \quad (\text{A.11})$$

Thus, if  $\rho(x, y, z)$  is such that

$$\rho(x, y, z) = \rho(-x, y, z) \quad \text{and} \quad \rho(x, y, z) = \rho(x, -y, z) \quad (\text{A.12})$$

or

$$\rho(x, y, z) = \rho(x, y, -z) \quad (\text{A.13})$$

we get

$$\mathbf{L} = m\boldsymbol{\omega} \int d\mathbf{r} (x^2 + y^2) \rho(\mathbf{r}) = \mathcal{I}\boldsymbol{\omega} \quad (\text{A.14})$$

In their classical paper on drops under surface tension, Brown and Scriven<sup>12</sup> have assumed that droplets have reflective symmetry about their equator plane ( $z = 0$ ), and at least one meridional plane of reflective symmetry (either  $x = 0$  or  $y = 0$ ). We have assumed that  $z = 0$  is a reflective plane of symmetry and have taken Eq. (A.14) for the definition of  $\mathbf{L}$ .



- 
- <sup>1</sup> C. Ebner and D.O. Edwards, *Phys. Rep.* **2C**, 77 (1970).
- <sup>2</sup> J.P. Toennies, *Annu. Rev. Phys. Chem.* **55**, 1 (2004).
- <sup>3</sup> K. K. Lehmann and G. Scoles, *Science* **279**, 2065 (1998).
- <sup>4</sup> J. P. Toennies and A. F. Vilesov, *Angew. Chem. Phys.* **43**, 2622 (2004).
- <sup>5</sup> B. G. Sartakov, J. P. Toennies, and A. F. Vilesov, *J. Chem. Phys.* **136**, 134316 (2012).
- <sup>6</sup> M. Barranco, R. Guardiola, S. Hernández, R. Mayol, J. Navarro, and M. Pi, *J. Low Temp. Phys.* **142**, 1 (2006).
- <sup>7</sup> F. Ancilotto, M. Barranco, F. Coppens, J. Eloranta, N. Halberstadt, A. Hernando, D. Mateo, and M. Pi, *Int. Rev. Phys. Chem.* **36**, 621 (2017).
- <sup>8</sup> R.M. Tanyag, C.F. Jones, C. Bernando, S.M. O’Connell, D. Verma, and A.F. Vilesov, in *Theoretical and Computational Chemistry Series No. 11*, O. Dulieu and A. Osterwalder editors. Royal Society of Chemistry, Cambridge, p. 389 (2018)
- <sup>9</sup> L.F. Gomez, K.R. Ferguson, J.P. Cryan, C. Bacellar, R.M.P. Tanyag, C. Jones, S. Schorb, D. Anielski, A. Belkacem, C. Bernando, R. Boll, J. Bozek, S. Carron, G. Chen, T. Delmas, L. Englert, S.W. Epp, B. Erk, L. Foucar, R. Hartmann, A. Hexemer, M. Huth, J. Kwok, S.R. Leone, J.H. S. Ma, F.R. N. C. Maia, E. Malmerberg, S. Marchesini, D.M. Neumark, B. Poon, J. Prell, D. Rolles, B. Rudek, A. Rudenko, M. Seifrid, K.R. Siefertmann, F.P. Sturm, M. Swiggers, J. Ullrich, F. Weise, P. Zwart, C. Bostedt, O. Gessner, and A.F. Vilesov, *Science* **345**, 906 (2014).
- <sup>10</sup> B. Langbehn, K. Sander, Y. Ovcharenko, C. Peltz, A. Clark, M. Coreno, R. Cucini, M. Drabbels, P. Finetti, M. Di Fraia, L. Giannessi, C. Grazioli, D. Iablonskyi, A.C. LaForge, T. Nishiyama, V. Oliver Álvarez de Lara, P. Piseri, O. Plekan, K. Ueda, J. Zimmermann, K.C. Prince, F. Stienkemeier, C. Callegari, T. Fennel, D. Rupp, and T. Möller, *Phys. Rev. Lett.* **121**, 255301 (2018).
- <sup>11</sup> O. Gessner and A.F. Vilesov, *Annu. Rev. Phys. Chem.* **70**, 173 (2019).
- <sup>12</sup> R.A. Brown and L.E. Scriven, *Proc. R. Soc. Lond. A* **371**, 331 (1980).
- <sup>13</sup> C.-J. Heine, *IMA J. Num. Anal.* **26**, 723 (2006)
- <sup>14</sup> S.L. Butler, M.R. Stauffer, G. Sinha, A. Lilly, and R.J. Spiteri, *J. Fluid Mech.* **667**, 358 (2011).
- <sup>15</sup> K.A. Baldwin, S.L. Butler, and R.J.A. Hill, *Sci. Rep.* **5**, 7660 (2015).
- <sup>16</sup> F. Ancilotto, M. Pi, and M. Barranco, *Phys. Rev. B* **97**, 184515 (2018).
- <sup>17</sup> D. Verma, S.M. O’Connell, A. Feinberg, S. Erukala, R.M. Tanyag, W. Pang, C. Saladrigas, B. Toulson, M. Borgwardt, N. Shivaram, M.-Fu Lin, A. Al Haddad, W. Jäger, C. Bostedt, P. Walter, O. Gessner, and A.F. Vilesov, submitted for publication (2019).
- <sup>18</sup> S. Stringari and J. Treiner, *J. Chem. Phys.* **87**, 5021 (1987).
- <sup>19</sup> D. Mateo, M. Pi, J. Navarro, and J. P. Toennies, *J. Chem. Phys.* **138**, 044321 (2013).
- <sup>20</sup> F. Garcias, Ll. Serra, M. Casas, and M. Barranco, *J. Chem. Phys.* **108**, 9102 (1998).
- <sup>21</sup> R. Guardiola and J. Navarro, *Phys. Rev. A* **71**, 035201 (2005).
- <sup>22</sup> M. P. de Lara-Castells, P. Villarreal, G. Delgado-Barrio, and A.O. Mitrushchenkov, *J. Chem. Phys.* **131**, 194101 (2009)
- <sup>23</sup> A. Leal, D. Mateo, M. Pi, M. Barranco, and J. Navarro, *J. Chem. Phys.* **139**, 174308 (2013).
- <sup>24</sup> B. Grammaticos, *Phys. Rev. C* **17**, 1244 (1978).
- <sup>25</sup> L. Münchow and H. Schulz, *J. Phys. G* **5**, 527 (1979).
- <sup>26</sup> B. Grammaticos and T. Sami, *J. Phys. G* **7**, 1063 (1981).
- <sup>27</sup> M. Barranco, M. Pi, S.M. Gatica, E.S. Hernández, and J. Navarro, *Phys. Rev. B* **56**, 8997 (1997).
- <sup>28</sup> R.J. Lombard, *Ann. Phys. (N.Y.)* **77**, 380 (1973).
- <sup>29</sup> A. deShalit and H. Feshbach, *Theoretical Nuclear Physics, Vol. I: Nuclear Structure*, (John Wiley & Sons, New York, 1974).
- <sup>30</sup> A. Bohr and B.R. Mottelson, *Nuclear Structure, Vol II*, (W.A. Benjamin, Reading, Massachusetts, 1975).
- <sup>31</sup> P. Ring and P. Schuck, *The Nuclear Many-Body Problem*, (Springer-Verlag, New York, 1980).
- <sup>32</sup> 4He-DFT BCN-TLS: A Computer Package for Simulating Structural Properties and Dynamics of Doped Liquid Helium-4 Systems. M. Pi, F. Ancilotto, F. Coppens, N. Halberstadt, A. Hernando, A. Leal, D. Mateo, R. Mayol, and M. Barranco, <https://github.com/bcntls2016/>
- <sup>33</sup> M. Barranco, F. Coppens, N. Halberstadt, A. Hernando, A. Leal, D. Mateo, R. Mayol, and M. Pi, <https://github.com/bcntls2016/DFT-Guide/blob/master/dft-guide.pdf>
- <sup>34</sup> K. Penanen, M. Fukuto, R.K. Heilmann, I.F. Silvera, and P.S. Pershan, *Phys. Rev.* **62**, 9621 (2000).
- <sup>35</sup> H. Lamb, *Hydrodynamics*, 6th. edition (Dover, New York, 1945).
- <sup>36</sup> We have analyzed the density profiles along the coordinate axes for some oblate and prolate configurations, and have found that surface diffuseness hardly depends on the deformation of the droplet.
- <sup>37</sup> C. Bernando, R.M.P. Tanyag, C. Jones, C. Bacellar, M. Bucher, K.R. Ferguson, D. Rupp, M. P. Ziemkiewicz, L.F. Gomez, A.S. Chatterley, T. Gorkhover, M. Müller, J. Bozek, S. Carron, J. Kwok, S.L. Butler, T. Möller, Ch. Bostedt, O. Gessner, and A.F. Vilesov, *Phys. Rev. B* **95**, 064510 (2017).
- <sup>38</sup> F. Ancilotto, M. Pi, and M. Barranco, *Phys. Rev. B* **91**, 100503(R) (2015).
- <sup>39</sup> S.M.O. O’Connell, R.M.P. Tanyag, D. Verma, Ch. Bernando, W Pang, C. Bacellar, C.A. Saladrigas, J. Mahl, B.W. Toulson, Y. Kumagai, P. Walter, F. Ancilotto, M. Barranco, M. Pi, Ch. Bostedt, O. Gessner, and A.F. Vilesov, submitted to *Phys. Rev. Lett.* (2019)